Experimental and numerical investigations on characteristics of coaxial liquid cone in coflow focusing

Kai Mu, Chunyu Zhang, Ting Si,* and Hang Ding
Department of Modern Mechanics, University of Science and Technology of China, Hefei 230026, China

(Received 8 September 2021; accepted 21 January 2022; published 7 February 2022)

The interfacial instability and flow patterns of coaxial liquid cone in a coflow focusing (CFF) process are investigated through the integration of experiments and numerical simulations. Based on the flow fields obtained quantitatively in numerical simulations, the startup process of focused coaxial liquid cone is established, and the streamlines of focusing stream are further compared with the potential flow model. The effects of main process parameters, including liquid flow rates, physical properties of materials, and geometrical parameters of CFF device on the cone morphologies, are given experimentally and numerically, and the local competition between the viscous shear stress and the interfacial tension on inner and outer cone interfaces is analyzed qualitatively through nondimensional parametric analysis. Moreover, through the particle tracing method in CFF experiments, the flow fields inside the liquid cone are obtained, with much attention paid to the recirculation flow occurring inside the inner liquid cone. The results show that the variation of liquid flow rates can manipulate the size of recirculation flow, and the balance of tangential shear stress makes main contributions to the formation of recirculation flow. This study provides significant guidance for the generation of microcapsules by the CFF technique in practical applications.

DOI: 10.1103/PhysRevFluids.7.024001

I. INTRODUCTION

Microcapsules often refer to the core-shell structured products at microscopic scales with one kind of material encapsulated in another phase of material, and have been widely applied in industrial fields such as pharmaceutics, material technology, food industry, and bioscience [1,2]. In recent decades, capillary flow methods have been popularly utilized for producing microcapsules, where the fluid interface is stretched to microscopic scale and ultimately breaks up into droplets due to the interface instability [3,4]. One of emerging capillary flows is called coflow focusing (CFF) [5–7], in which three phases of immiscible fluids flow through the focusing orifice simultaneously, forming a steady coaxial liquid cone-jet configuration in the focusing stream. In comparison with the traditional microfluidic systems in which the flow velocity is relatively low due to the geometrical restriction of solid wall boundaries [8–13], the CFF method can lead to much faster flow velocity and thus has high throughput in generating microcapsules [14–16].

The pioneering study of CFF was carried out by Gañán-Calvo [17], where a coaxial ink-in-oil jet is formed in the high speed gas environment. In the CFF process, the innermost core fluid and the interlayered shell fluid are selected as two immiscible liquids, and the selection of outermost focusing fluid can be either gaseous phase or liquid phase. There are two most typical modes for the generation of compound droplets, the jetting and dripping modes [5,7,14]. In the jetting mode, a steady coaxial cone-jet configuration can be established with droplets formed some distance

*tsi@ustc.edu.cn

away from the focusing orifice; while in the dripping mode, the compound droplets are produced at the exit of orifice with either a stable or an unstable coaxial cone. Generally, the jetting mode occurs at relatively large values of liquid flow rates, and the jet can be maintained under the joint contribution of inertia and shear stress. As the liquid flow rates gradually decrease, the jetting mode can convert to the dripping mode, in which the evolution of interfaces is dominated by the interfacial tension [7]. The transition boundary between jetting and dripping modes can be theoretically predicted through linear instability analysis on the spatiotemporal development of initial infinitesimal disturbances [5,18]. In practical applications, the jetting mode is more commonly utilized for producing microcapsules due to its higher breakup frequency and smaller droplet size comparing with the dripping mode [6,15,16]. To control the breakup of coaxial liquid jets, external mechanical stimulations can be further applied on the CFF process, enhancing the monodispersity of resultant compound droplets and suppresses the formation of satellite droplets [19,20]. Moreover, the size and geometrical structure of the compound droplets can be manipulated by adjusting the frequency and waveform of the mechanical stimulations [21]. Recently, the breakup of coaxial liquid jets is also studied through numerical simulations [22–24], which illustrate more detailed characteristics of coaxial liquid jets and resultant microdroplets, and provide quantitative flow fields to access the underlying mechanism of the breakup of coaxial liquid jets.

It should be emphasized that a stable coaxial liquid cone upstream the orifice is the precondition for the establishment of a coaxial liquid jet, which guarantees the efficient production of compound droplets. In previous studies, the interface morphologies of coaxial liquid cone were observed for the outermost focusing fluid of either gas [25] or liquid [26]. However, to the best of our knowledge, a systematic consideration on the interfacial instability and flow patterns of coaxial liquid cone is still lacking, although the single liquid cone in single-axial flow focusing (SFF) has been studied extensively [27–29]. In comparison with the SFF process, the addition of the second cone interface and the complexity of more process parameters in CFF would bring in much more phenomena that should be understood to produce microcapsules for potential applications. Therefore, a comprehensive study on the interfacial instability and flow patterns of coaxial liquid cone is desired, especially by considering the influences of various process parameters such as liquid flow rates, physical properties of materials and geometrical parameters of CFF device.

In this work, we aim to perform a parametric study on the coaxial liquid cone in the liquid-driven CFF process through experiments and numerical simulations. The dynamic startup process of the cone interface under the driving effect of focusing stream is first given. Once the coaxial liquid cone is established, a nondimensional analysis is performed to show the effects of main process parameters on the stability of the inner and outer liquid cones. The theoretical prediction is validated qualitatively by the experimental and numerical results. The flow fields inside the liquid cone are then studied through the particle tracing method and numerical simulations, showing the underlying mechanism for the appearance of recirculation flows. Finally, the main conclusions are drawn.

II. EXPERIMENTAL AND NUMERICAL METHODS

In CFF experiments, two immiscible liquids of the core phase (liquid 1: density ρ_1, viscosity μ_1, flow rate Q_1) and the shell phase (liquid 2: density ρ_2, viscosity μ_2, flow rate Q_2) flow out of the coaxial needle continuously within the chamber, and get focused by the focusing stream (liquid 3: density ρ_3, viscosity μ_3, flow rate Q_3) at the orifice facing directly to the coaxial needle, forming the coaxial liquid cone-jet configuration, as shown in Fig. 1(a). The diameters of the inner and outer needles are denoted by D_1 and D, and the diameter and thickness of the orifice are denoted by d and T, respectively. The distance between the orifice and the outer needle is H, and the inner tube outset is h. In our experiments, we keep the geometrical parameters constant, set as $D = 1050$ μm, $D_1 = 420$ μm, $d = 840$ μm, $T = 450$ μm, H varies between 0.5 and 1.5 mm and h varies between 0 and 0.5 mm. Distilled water is chosen as the core and focusing liquids, and silicone oil is chosen as the shell liquid. The physical properties of materials are $\rho_1 = \rho_3 = 996$ kg m^{-3}, $\mu_1 = \mu_3 = 0.001$ Pa s, $\rho_2 = 965$ kg m^{-3} and $\mu_2 = 0.04$ Pa s, and the interfacial tension between water and oil is $\sigma = 32.8$

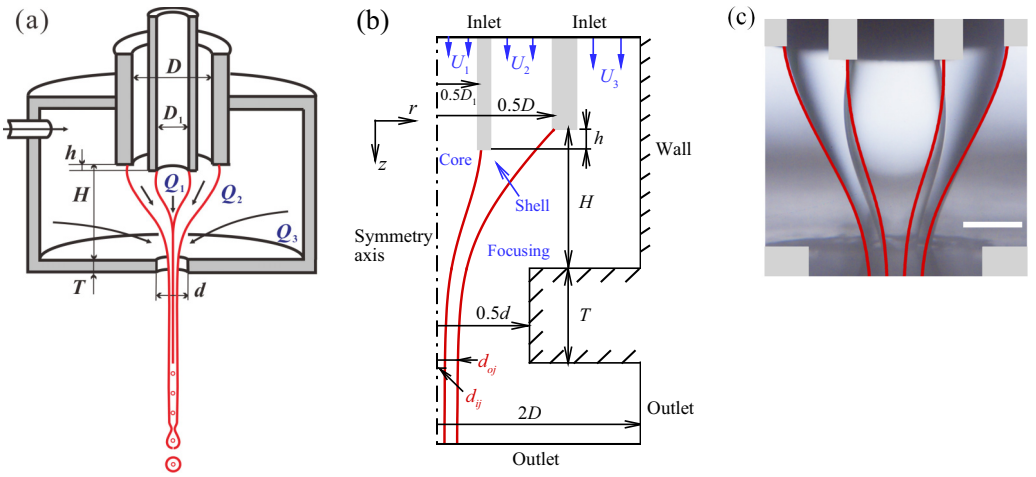

FIG. 1. (a) Sketch of the CFF device showing the geometric parameters and the interface profiles of the steady coaxial cone-jet configuration. (b) Computational domain for numerical simulations, where U_1, U_2, and U_3 stand for the inlet flow velocities of core, shell and focusing phases, respectively. (c) Comparison between the experimental and numerical results of the coaxial cone at the liquid flow rates of $Q_1 = 15$ ml/h, $Q_2 = 100$ ml/h and $Q_3 = 1400$ ml/h. The experimental inner liquid cone seems enlarged because of the optical refraction effect arising from the presence of the outer liquid cone. Scale bar: 300 μm.

mN m^{-1}. The evolution of liquid interfaces is recorded by a high-speed video camera (Photron, Fastcam Mini AX 200, Japan) equipped with a microscope (Leica Z16 APO, Germany) under the illumination of an intense light source (Sumita LS-M352, Japan) from the other side of the chamber. A frosted diffuser is placed in front of the light source, which transforms the quasi-parallel light to diverging light and realizes the quasi-uniform illumination in the field of view. The high-speed camera is connected to a computer for data recording and post processing.

In numerical simulations, the computational domain of CFF is presented in Fig. 1(b). The geometric parameters, boundary conditions and averaged inlet flow velocities U_1, U_2, and U_3 are also indicated. In this work, we mainly focus on the interfacial instability and flow patterns of coaxial liquid cone located between the coaxial needle and the focusing orifice. As the breakup of coaxial liquid jets to compound droplets far away from the orifice is beyond the focus of current work, the computation domain downstream the orifice is chosen much shorter than the real situation to minimize the calculation cost. For better capturing the fluid interfaces and the flow fields, a ternary-fluid diffuse-interface model proposed in our group [30] is utilized to directly solve the Navier-Stokes equations, where the interface is represented by the volume fraction of the liquid C, and its time evolution is governed by the Cahn-Hilliard equation [31,32],

$$\frac{\partial \mathbf{C}}{\partial t} + \nabla \cdot (\mathbf{uC}) = \frac{1}{\mathrm{Pe}} \nabla^2 (\mathbf{\Psi} - C_1 C_2 C_3), \tag{1}$$

where $\mathbf{u}$ is the liquid velocity and $\mathbf{C} = (\mathbf{C_1}, \mathbf{C_2})$ is the volume fraction of liquids 1 and 2, respectively. The volume fraction of liquid 3 can be calculated as $C_3 = 1 - C_1 - C_2$. In our simulations of CFF, liquid 1, 2, and 3 indicate the core, shell, and focusing liquids, respectively. The Peclet number Pe represents the ratio of the convective flux to the diffusive flux, and the chemical potential $\mathbf{\Psi} = (\psi_1, \psi_2)$ is defined by the variation of free energy with respect to the volume fraction $\mathbf{C}$ with the form

$$\psi_i = \frac{\partial F(C_i)}{\partial C_i} - \mathrm{Cn}^2 \nabla^2 C_i, \quad i = 1, 2, \tag{2}$$

where $F(C_i) = \frac{1}{4}C_i^2(1-C_i)^2$ is the bulk energy density, and the Cahn number Cn is a dimensionless measurement of the diffuse interface thickness. A larger value of Cn results in a thicker interface, but the calculation of interfacial tension is more accurate as there are more meshes to resolve the interface. To guarantee the calculation accuracy under a relatively thin interface, we set $\mathrm{Cn} = 0.5\Delta x$ where Δx is the mesh size. The Peclet number is set to $\mathrm{Pe} = 1/\mathrm{Cn}$ to ensure the convergence of the diffuse interface. We expand $\partial F(C_i)/\partial C_i$ to get

$$\begin{aligned}\frac{\partial F(C_i)}{\partial C_i} &= \frac{1}{2}C_i(1-C_i)^2 - \frac{1}{2}C_i^2(1-C_i),\\ &= \frac{1}{2}\left(C_i - 2C_i^2 + C_i^3 - C_i^2 + C_i^3\right),\\ &= \frac{1}{2}\left(2C_i^3 - 3C_i^2 + C_i\right),\\ &= C_i^3 - 1.5C_i^2 + 0.5C_i. \end{aligned} \tag{3}$$

Then the expression of Eq. (2) can then be written as

$$\psi_i = C_i^3 - 1.5C_i^2 + 0.5C_i - \mathrm{Cn}^2\nabla^2 C_i, \quad i = 1, 2. \tag{4}$$

The motion of the liquids is governed by the dimensionless Navier-Stokes equations [33],

$$\rho\left(\frac{\partial \mathbf{u}}{\partial t} + \mathbf{u}\cdot\nabla\mathbf{u}\right) = -\nabla p + \frac{1}{\mathrm{Re}}\nabla\cdot[\mu(\nabla\mathbf{u} + \nabla\mathbf{u}^T)] + \frac{\mathbf{f}_s}{\mathrm{We}}, \tag{5}$$

$$\nabla\cdot\mathbf{u} = 0, \tag{6}$$

where ρ and μ are the dimensionless density and viscosity, respectively, which are defined as

$$\rho = C_2 + \frac{\rho_1}{\rho_2}C_1 + \frac{\rho_3}{\rho_2}C_3, \tag{7}$$

$$\mu = C_2 + \frac{\mu_1}{\mu_2}C_1 + \frac{\mu_3}{\mu_2}C_3, \tag{8}$$

with ρ_i and μ_i the density and viscosity of fluid i ($i = 1, 2, 3$), respectively. $\mathbf{f}_s$ represents the interfacial tension force and is computed as

$$\mathbf{f}_s = \frac{3\sqrt{2}}{\sin\varphi_1}\sum_{i=1}^{3}\alpha_i\psi_i\nabla C_i. \tag{9}$$

Here, $\alpha_1 = \sin\varphi_3 - \sin\varphi_1 + \sin\varphi_2$, $\alpha_2 = \sin\varphi_3 + \sin\varphi_1 - \sin\varphi_2$, and $\alpha_3 = \sin\varphi_1 + \sin\varphi_2 - \sin\varphi_3$, and φ_i denote the interfacial angles which are decided by the interfacial tension of interfaces,

$$\frac{\sin\varphi_1}{\sigma_2} = \frac{\sin\varphi_2}{\sigma_3} = \frac{\sin\varphi_3}{\sigma_1}, \tag{10}$$

where σ_2, σ_3, and σ_1 denote the interfacial tension coefficient between liquids 2 and 3, liquids 3 and 1, and liquids 1 and 2, respectively. In CFF process, the interfacial tensions of the inner cone (inner interface) and the outer cone (outer interface) correspond to σ_1 and σ_2, respectively.

In our simulations, we choose D and U_2 of the shell liquid (liquid 2) as the characteristic length and velocity, thus the Reynolds number $\mathrm{Re} = \rho_2 U_2 D/\mu_2$ and the Weber number $\mathrm{We} = \rho_2 U_2^2 D/\sigma_2$ can be defined. All the computations are performed under a mesh size $\Delta x = 0.0025D$. For the convenience of analysis, we also refer to the Ohnesorge number $\mathrm{Oh} = \mu_2/\sqrt{\rho_2\sigma_2 D}$. The flow rates of core and focusing liquid are reflected by the flow rate ratio $q_1 = Q_1/Q_2$ and $q_2 = Q_3/Q_2$, respectively. The density ratios $r_{\rho 1} = \rho_1/\rho_2$ and $r_{\rho 2} = \rho_3/\rho_2$, viscosity ratios $r_{\mu 1} = \mu_1/\mu_2$ and $r_{\mu 2} = \mu_3/\mu_2$, and interfacial tension ratio $r_\sigma = \sigma_1/\sigma_2$ can also be defined. In this work, the referenced dimensionless parameters corresponding to the experimental conditions are $\mathrm{Oh} = 0.208$, $r_{\rho 1} = r_{\rho 2} = 1.03$, $r_{\mu 1} = r_{\mu 2} = 0.025$, and $r_\sigma = 1$. The values of We, q_1, and q_2 all vary with the

liquid flow rates. For the numerical simulations, we will further study the effects of liquid viscosities and interfacial tension through changing Oh, $r_{\mu 2}$, and r_σ.

The boundary conditions for the flow velocity are implemented as follows: $v = 0$, $\partial u/\partial r = 0$ at the symmetry axis $r = 0$, where u and v are the r and z components of the velocity, respectively; no-slip condition ($u = 0$ and $v = 0$) at the solid wall; $u = 0$ and $v = v_{\text{in}}$ at the inlet, where $v = v_{\text{in}}$ is a prescribed value which is determined by the liquid flow rates; $\partial u/\partial z = 0$ and $\partial v/\partial t + v(\partial v/\partial z) = 0$ at the downside outlet; $\partial v/\partial r = 0$ and $\partial u/\partial t + u(\partial u/\partial r) = 0$ at the rightside outlet. The numerical code has been validated successfully in our previous studies [7,23,30]. For more information, we present a comparison between the numerical results and experimental observations of the coaxial liquid cone, as shown in Fig. 1(c). The flow rates are $Q_1 = 15$ ml/h, $Q_2 = 100$ ml/h, and $Q_3 = 1400$ ml/h, which correspond to We $= 0.04$, $q_1 = 0.15$, and $q_2 = 14$, respectively. It can be easily seen that a good agreement can be reached for the interface profile of outer liquid cone. Due to the optical refraction effect arising from the presence of the outer liquid cone, the experimental inner liquid cone seems enlarged in comparison with the numerical results, which would be hardly avoided in experimental observations. Moreover, we find that the cross section of the inner and outer capillary tube is not totally flat and there exists a certain degree of contact angle hysteresis in experiments. These limitations will affect the anchorage of the contact line at the capillary tube, causing the discrepancy between experimental and numerical results. Since an acceptable agreement can be reached, the numerical simulations will be utilized for providing more detailed information of curved inner cone interfaces and flow fields.

III. RESULTS AND DISCUSSION

A. Startup process of the coaxial liquid cone

In a typical startup process of CFF, the flows of triple liquids are generally supplied by initially injecting the outermost focusing phase to maintain the stable bulk flow within the chamber, and then the shell phase to form a stable single liquid cone, and eventually the core phase to form a stable coaxial liquid cone-jet configuration. The preferential injection of focusing liquid can provide constant velocity field for the surrounding flow close to the orifice, which avoids the adhesion of focused outer and inner liquids to the solid wall and contributes to the formation of cone configuration upstream the orifice. As the quantitative flow fields are hard to be measured in experiments due to the small size and three-dimensional structure of coaxial liquid cone, we utilize numerical tools to study the startup process of the outer and inner liquid cones.

As the focusing liquid is first injected into the chamber, the flow fields for the flow after maintaining its steady state are shown in Fig. 2(a), where the streamlines and the dimensionless values of pressure field (denoted by P) and flow velocity (denoted by V) are given in the left and right part, respectively. It is clearly seen that as the streamlines gradually converge close to the orifice, the flow velocity increases significantly while the pressure decreases with velocity increasing. Moreover, the boundary layer occurs along the side wall of the orifice [see the right part of Fig. 2(a)], where the axial velocity quickly decreases to zero at the side wall of orifice. Actually, the streamlines for the single focusing liquid were predicted theoretically through the potential flow model in previous studies on SFF [34,35]. In this work, we further compare the potential flow model with numerical results. Figure 2(a) presents the comparison between the theoretical prediction (see Eq. (1) in Acero *et al.* [34]) with the numerical simulation, where the streamlines obtained theoretically and numerically are denoted by dashed and arrowed solid lines, respectively. Overall, a good agreement can be reached between the theoretical results and numerical simulations, except that some deviation exists close to the orifice. As the potential flow approximation assumes the inviscid and irrotational flow across a zero-thickness orifice, the streamlines at the orifice are totally perpendicular to the orifice plate. However, the orifice with finite thickness in numerical simulation leads to nonnegligible boundary layer effect at the side wall of orifice, which causes the streamlines at the orifice diverging from the theoretical results. Moreover, the inertia of liquid

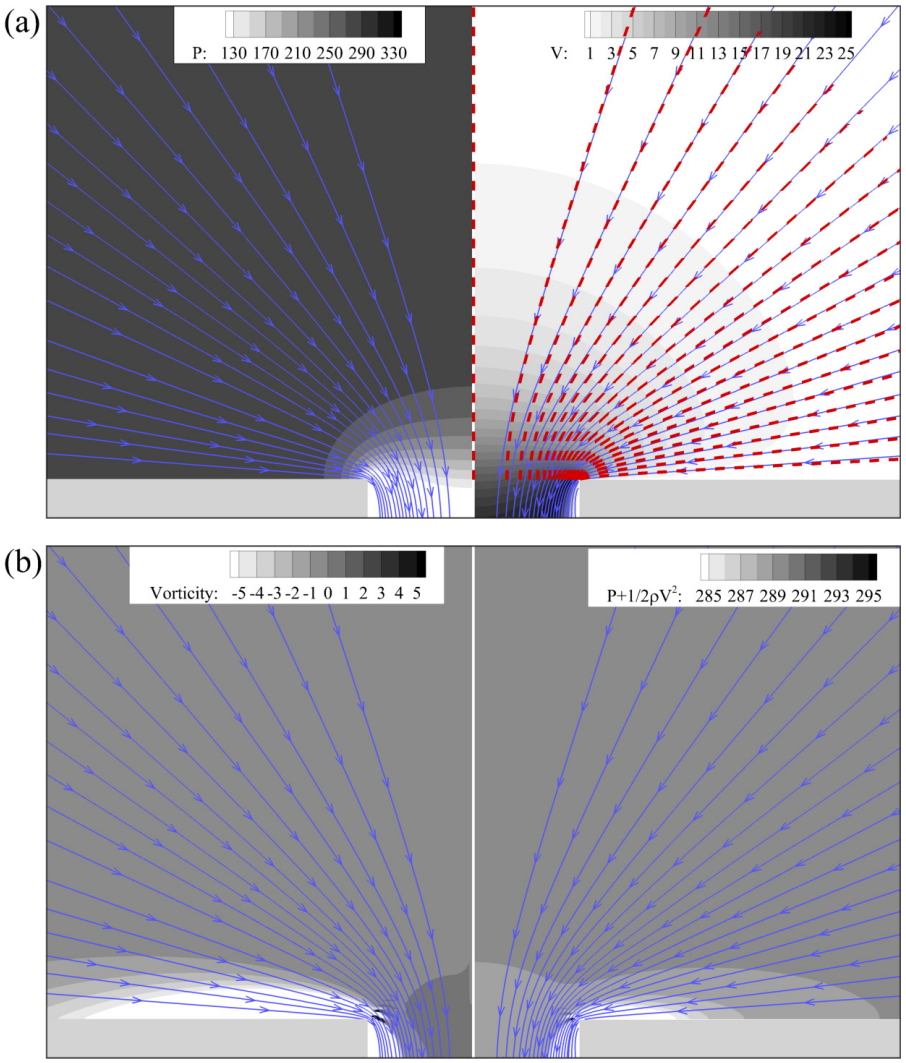

FIG. 2. (a) Dimensionless pressure and velocity field of focusing liquid and comparison between potential flow model [34] (dashed lines) and numerical simulation (arrowed solid lines) on the streamlines. (b) Dimensionless vorticity field and the value of $(P + 1/2\rho V^2)$ of focusing liquid.

during the convergence at the orifice can also lead to radial velocity, thus the streamlines obtained through numerical simulations are not perpendicular to the orifice.

To further explain the rationality of potential flow model in theoretical analysis, Fig. 2(b) gives the dimensionless vorticity field close to the focusing orifice (see the left part). It is observed that the value of vorticity is close to zero except that at the position very close to the solid wall, suggesting the approximate irrotational characteristic of focusing flow. The right part of Fig. 2(b) further gives the dimensionless value of $(P + 1/2\rho V^2)$ which is calculated by the pressure and flow velocity. Similar to the results of vorticity field, the value of $(P + 1/2\rho V^2)$ approximates a constant value except that at the position close to the solid wall. This observation suggests the reasonability of Bernoulli equation along the streamlines. Therefore, the inviscid assumption in the potential flow model is also well satisfied. Actually, previous work has successfully predicted the jet diameter in SFF based on the Bernoulli equation [17]. Overall, the numerical simulations further demonstrate

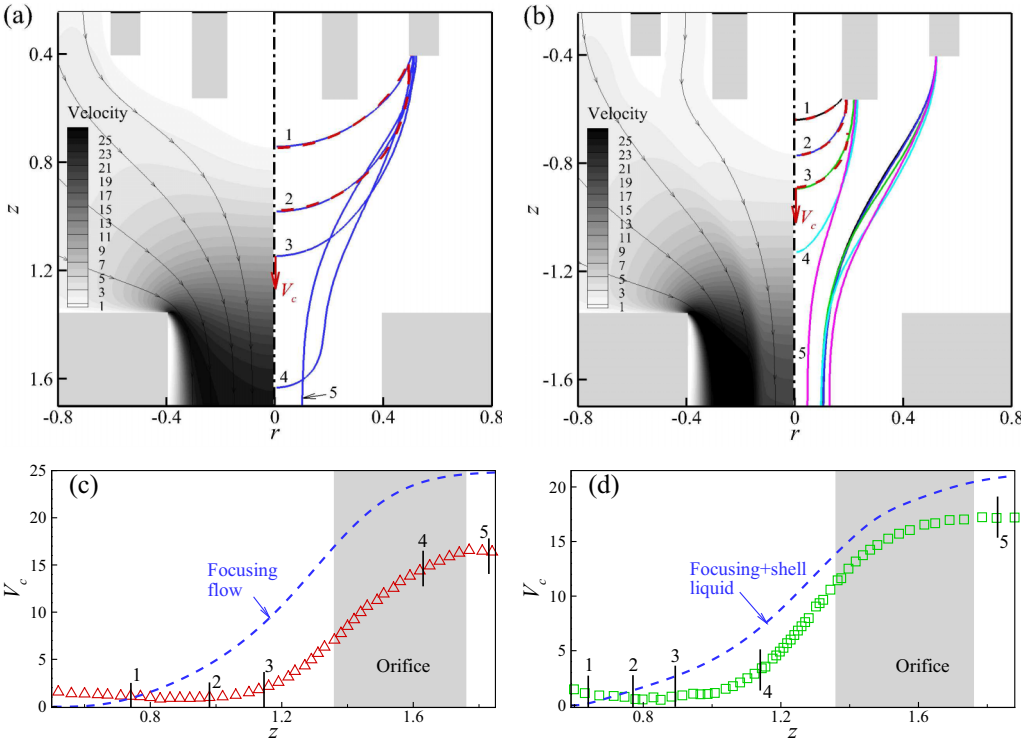

FIG. 3. (a) The velocity field of the focusing flow after maintaining its steady state without the shell and core fluids (left part) and the shell liquid interface profiles showing the startup process on the formation of outer liquid cone (right part). The red dashed lines denote the spherically fitted profiles for the interface. (b) The velocity field after the establishment of a steady outer liquid cone under the focusing flow (left part) and the shell and core liquid interfaces showing the startup process on the formation of inner liquid cone (right part). (c) The apex velocity V_c measured at the interface tip of the outer cone at different z position during the startup process of outer liquid cone. For comparison, the dashed line gives the velocity distribution for pure steady focusing flow along the center line. (d) V_c measured at the interface tip of the inner cone at different z position. The dashed line gives the velocity distribution for the combination of focusing and shell flows along the center line in steady state.

that the potential flow model is reasonable to give a good prediction of the focusing flow field in different methods based on flow focusing principle.

In CFF process, the velocity field for the steady focusing flow is shown in the left part of Fig. 3(a), where the streamlines and the dimensionless values of flow velocity are given simultaneously. It is notable that the addition of coaxial capillary tube only change the velocity field slightly comparing with the results in Fig. 2(a). The process parameters here are chosen to ensure the formation of a stable coaxial liquid cone when three fluids are supplied continuously. The right part of Fig. 3(a) shows the startup process of outer liquid cone for the shell liquid in the steady focusing flow. When the cone interface is far from the orifice (e.g., profiles 1 and 2), the stretching effect of the focusing flow is very weak as the local flow velocity is almost negligible; therefore, the shell liquid cone maintains an approximate spherical profile under the effect of interfacial tension. For comparison, the spherically fitted profiles for the cone interface are plotted by red dashed lines in Fig. 3(a). As the shell liquid interface gradually approaches the orifice, it is quickly stretched under the shearing stress of the focusing flow (profiles 3 and 4) and finally forms a stable cone profile (profile 5).

To show the characteristics of interface movement, the velocity of the shell liquid interface tip (denoted by V_c) with the variation of axial coordinates z is given in Fig. 3(c), which verifies the obvious acceleration of interface as it evolves close to the orifice (e.g., $z > 1$). It is notable that the value of V_c is obviously lower than that of axial velocity of focusing flow measured along the symmetric axis when there is only steady focusing flow as the shell liquid is not supplied (see the dashed line), due to the inertia of the shell liquid during the acceleration process. Similar to the formation of outer liquid cone, the formation process of inner liquid cone is shown in Fig. 3(b), where the stationary velocity field after the establishment of a stable outer liquid cone is given in the left part and the evolution of inner and outer interfaces is shown in the right part, respectively. Since the flow velocity away from the orifice is relatively low (e.g., $z < 1$), the inner interface can maintain the approximate spherical profile (profiles $1 \sim 3$, spherically fitted by the red dashed lines). As the interface evolves close to the orifice, it gets stretched (profile 4) with its tip accelerating significantly. This tendency is clearly shown in Fig. 3(d), where the tip velocity V_c of the inner cone is given under different axial coordinates z. Likewise, V_c is lower than the axial velocity measured at the symmetric axis when only the steady focusing and the shell flows exist, as shown by the dashed line in Fig. 3(d). Finally, the inner interface is stretched sufficiently under the shear effect of the shell liquid and a stable inner cone can be established (profile 5). In the startup process of inner liquid cone, the profile of outer interface has slight variation as the total value of shell and core liquid flow rates increases. When the stable coaxial liquid cone is maintained (profile 5), the diameter of outer liquid jet issuing from the tip of the cone is enlarged, as illustrated in Fig. 3(b).

B. Nondimensional analysis on the cone instability

It has been clearly shown in Fig. 2 that the converging flow close to the orifice leads to obvious downstream pressure gradient. Moreover, the liquid acceleration caused by the pressure gradient brings in the effect of viscous shear stress, which is able to stretch the interface and contributes to the formation of a stable liquid cone. The stability of cone interface is found to be heavily dependent on the relative importance of viscous shear stress and the interfacial tension [36]. For the coaxial liquid cone in CFF, it can be simply considered that the outer cone is established under the shear stress of focusing flow and the inner cone is established under the shear stress of shell liquid, respectively, as the velocity gradient upstream the orifice can accelerate the interfaces to form the coaxial cone configuration (see the results shown in Fig. 3). Therefore, the instability of coaxial liquid cone can be analyzed by decoupling the outer and inner cone interfaces and considering the competition between viscous shear stress and interfacial tension of each interface. For the liquid cone in SFF studied previously, the instability of the single liquid cone is directly related to the global instability of the interface [28,37], where a temporally steady profile of liquid cone corresponds to the globally stable mode while a periodically vibrating profile between the orifice and the capillary tube corresponds to the globally unstable mode. Some theoretical global instability analyses have been carried out in past decade, showing the stability map of different flow modes [26,38–40]. The effect of various parameters on the cone instability in SFF has been studied through nondimensional analysis, in which the competition between the viscous shear stress and the interfacial tension on the cone interface is considered [29]. To quantify the relative value between the shear stress and the interfacial tension, the capillary number can be similarly defined in terms of the local effective elongation rate G as described in literatures [10,41,42]. For the outer liquid cone, the effective elongation rate G_o is defined as $G_o = \Delta V_o/H$ based on the focusing liquid, where ΔV_o is the difference between the upstream velocity and the local velocity inside the orifice. As the value of upstream velocity is negligible comparing with that in the orifice [see Fig. 3(a)], $\Delta V_o \approx 4Q_3/(\pi d^2)$ can be approximately obtained. Choosing the diameter of outer jet d_{oj} as the characteristic length, the capillary number is given by $\mathrm{Ca}_o = \mu_3 G_o d_{oj}/\sigma_2$. Similarly, the effective elongation rate G_i for the inner liquid cone can be defined based on flow of the shell liquid, which gives $G_i = \Delta V_i/(H - h) \approx 4Q_2/[\pi d_{oj}^2(H - h)]$. Therefore, the capillary number for the inner cone is given by $\mathrm{Ca}_i = \mu_2 G_i d_{ij}/\sigma_1$, where d_{ij} is the diameter of inner jet.

Previous studies on the coaxial jet have indicated that an approximated average velocity of the core, shell, and focusing liquid could be reached downstream the orifice due to the viscous momentum diffusion [23,43,44], which gives the prediction of jet diameters through volume conservation,

$$d_{oj} \approx d\left(\frac{Q_1+Q_2}{Q_1+Q_2+Q_3}\right)^{\frac{1}{2}} = d\left(\frac{1+q_1}{1+q_1+q_2}\right)^{\frac{1}{2}},$$
$$d_{ij} \approx d\left(\frac{Q_1}{Q_1+Q_2+Q_3}\right)^{\frac{1}{2}} = d\left(\frac{q_1}{1+q_1+q_2}\right)^{\frac{1}{2}}. \tag{11}$$

Under the assumption of $Q_1 \ll Q_2 \ll Q_3$ for most cases, we can obtain the capillary numbers for outer and inner liquid cones as

$$\mathrm{Ca}_o \approx \frac{\mu_3}{\sigma_2 dH}(Q_1+Q_2)^{\frac{1}{2}}Q_3^{\frac{1}{2}} = \frac{\mu_3}{\sigma_2 dH}Q_2^{\frac{1}{2}}Q_3^{\frac{1}{2}},$$
$$\mathrm{Ca}_i \approx \frac{\mu_2}{\sigma_1 d(H-h)}Q_1^{\frac{1}{2}}\frac{Q_2}{Q_1+Q_2}(Q_1+Q_2+Q_3)^{\frac{1}{2}} = \frac{\mu_2}{\sigma_1 d(H-h)}Q_1^{\frac{1}{2}}Q_3^{\frac{1}{2}}. \tag{12}$$

The dimensionless form gives

$$\mathrm{Ca}_o \approx \frac{r_{\mu 2}\mathrm{Oh}(\mathrm{We}q_2)^{\frac{1}{2}}}{\bar{d}\bar{H}}, \quad \mathrm{Ca}_i \approx \frac{\mathrm{Oh}(\mathrm{We}q_1q_2)^{\frac{1}{2}}}{r_\sigma \bar{d}(\bar{H}-\bar{h})}. \tag{13}$$

It can be found that the value of Ca_o is appropriately proportional to the square root of Q_2 and Q_3 (nondimensionalized as We and q_2), proportional to μ_3 (nondimensionalized as $r_{\mu 2}$), and inversely proportional to σ_2 (nondimensionalized as Oh) and the geometrical parameters of d and H (nondimensionalized as $\bar{d}$ and $\bar{H}$). The results indicate that, as the values of Q_2, Q_3, and μ_3 increase, or those of σ_2, d, and H decrease, the interfacial tension would play a less significant role at the outer liquid cone, making the cone much more stable. Moreover, the value of Ca_i is appropriately proportional to the square root of Q_1 and Q_3 (nondimensionalized as q_1 and q_2), proportional to μ_2 (nondimensionalized as Oh), and inversely proportional to σ_1 (nondimensionalized as r_σ) and the geometrical parameters of d, H, and h (nondimensionalized as $\bar{d}$, $\bar{H}$, and $\bar{h}$). As the values of Q_1, Q_3, and μ_2 increase, or those of σ_1, d, and $H-h$ decrease, the interfacial tension would play a less significant role for the inner liquid cone, promoting the formation of a stable cone.

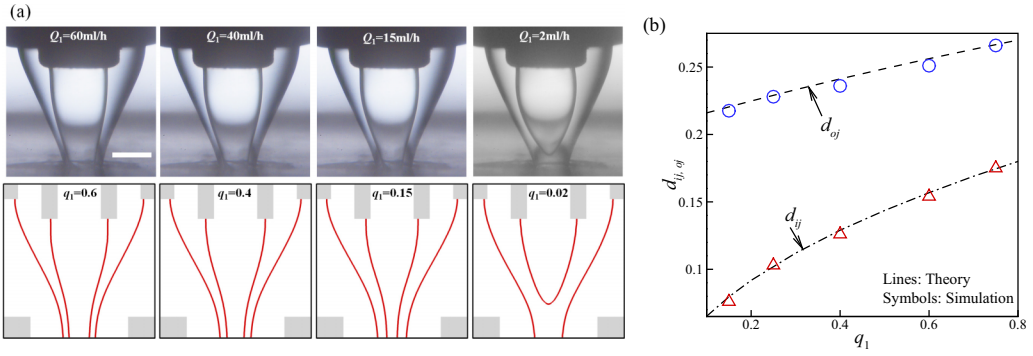

FIG. 4. (a) Coaxial liquid cone profiles as Q_1 changes at certain $Q_2 = 100$ ml/h and $Q_3 = 1400$ ml/h, corresponding to the variation of q_1 at certain $\mathrm{We} = 0.04$ and $q_2 = 14$. Scale bar: 300 μm. (b) The dimensionless inner and outer jet diameters (denoted by d_{ij} and d_{oj}, respectively) as q_1 varies. The dashed and dash-dotted lines denote the theoretical predictions of Eq. (11), respectively.

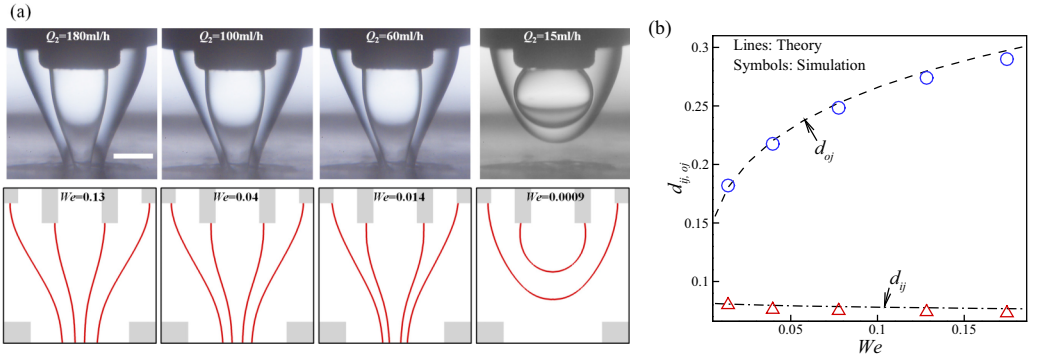

FIG. 5. (a) Coaxial liquid cone profiles as Q_2 changes at certain $Q_1 = 15$ ml/h and $Q_3 = 1400$ ml/h, corresponding to the variation of We at certain $\mathrm{We}q_1^2 = 0.009$ and $\mathrm{We}q_2^2 = 7.76$. Scale bar: 300 μm. (b) The dimensionless inner and outer jet diameters (d_{ij} and d_{oj}) as We varies. The dashed and dash-dotted lines denote the theoretical predictions of Eq. (11), respectively.

C. Effect of process parameters on the characteristics of the coaxial liquid cone

In this section, the effects of various process parameters on the instability and morphology of coaxial liquid cone are given in detail based on experimental and numerical results. It has been indicated in Eq. (12) that the cone instability is affected by the liquid flow rates, physical properties of materials and geometrical parameters of CFF device conjointly. For easy understanding, we will consider the effects of main contributing parameters, including the flow rates of core, shell and focusing liquids (Figs. 4–6), the geometrical parameters (Figs. 7–9), and the liquid physical properties (Figs. 10 and 11), respectively.

The core liquid flow rate Q_1 (nondimensionalized as q_1) is first considered in Fig. 4(a), in which the experimental and numerical results are located at the upper and lower part of each sub-graph. Once the liquid cone gets stable at large Q_1, a steady coaxial liquid jet can be formed with a certain diameter at the orifice, and the profile of inner cone gets more bulgy as Q_1 increases. However, as the value of Q_1 is lower than a critical value (e.g., $Q_1 = 2$ ml/h), the inner cone is unstable and vibrates between the capillary tube and the orifice. The result is consistent with the theoretical prediction of Eq. (12). The vibration of inner cone has little influence on the stability of outer liquid cone, and

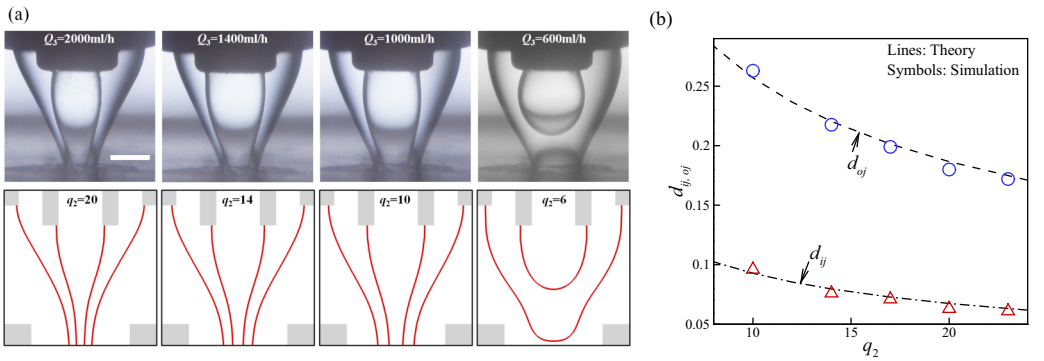

FIG. 6. (a) Coaxial liquid cone profiles as Q_3 changes at certain $Q_1 = 15$ ml/h and $Q_2 = 100$ ml/h, corresponding to the variation of q_2 at certain $q_1 = 0.15$ and $\mathrm{We} = 0.04$. Scale bar: 300 μm. (b) The dimensionless inner and outer jet diameters (d_{ij} and d_{oj}) as q_2 varies. The dashed and dash-dotted lines denote the theoretical predictions of Eq. (11), respectively.

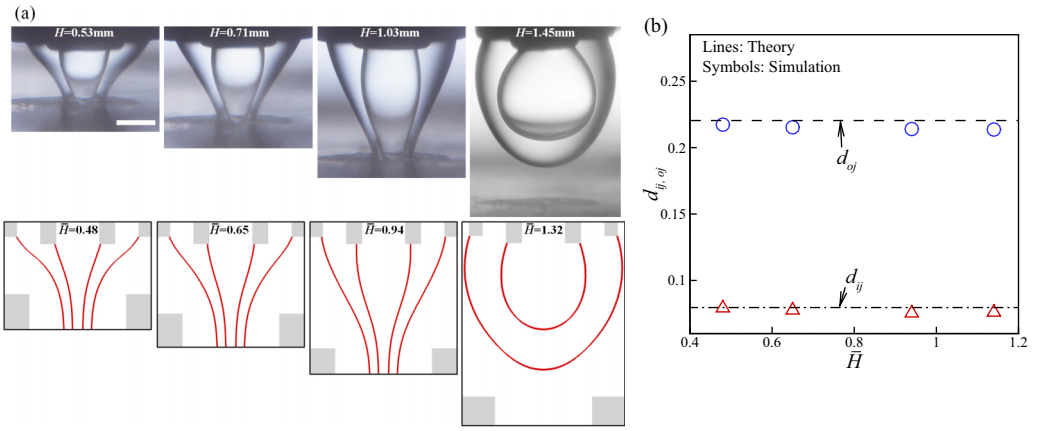

FIG. 7. (a) Coaxial liquid cone profiles as H (nondimensionalized as $\bar{H}$) varies at certain $Q_1 = 15$ ml/h, $Q_2 = 100$ ml/h and $Q_3 = 1400$ ml/h ($q_1 = 0.15$, We $= 0.04$ and $q_2 = 14$). Scale bar: 300 μm. (b) The dimensionless inner and outer jet diameters (d_{ij} and d_{oj}) as $\bar{H}$ varies. The dashed and dash-dotted lines denote the theoretical predictions of Eq. (11), respectively.

terminates the continuous formation of coaxial liquid jets downstream the orifice. Figure 4(b) plots the dimensionless outer and inner jet diameters [denoted by d_{oj} and d_{ij}, respectively; as sketched in Fig. 1(b)] of coaxial liquid jets measured at the orifice exit for stable coaxial liquid cone. Due to the optical distortion effect on the measurement of inner jet diameter in experiments, we only present the numerical results, showing a good agreement with the theoretical prediction of Eq. (11). Figure 5(a) considers the variation of shell liquid flow rate Q_2 (nondimensionalized as We). It is notable that according to the definition of the dimensionless parameters, the variation of Q_2 at certain Q_1 and Q_3 corresponds to the change of We under fixed values of $\mathrm{We}q_1^2$ and $\mathrm{We}q_2^2$. The coaxial liquid cone is always stable for large value of Q_2. As Q_2 is lower than a critical value, the coaxial liquid cone gets unstable. According to Eq. (12), the decrease of Q_2 mainly affects the instability of the outer cone. Once the outer cone is unstable, the vibration of the outer interface would certainly cause the accompanying vibration of the inner liquid cone. Figure 5(b) plots the numerical results of the dimensionless outer and inner jet diameters measured at the orifice exit,

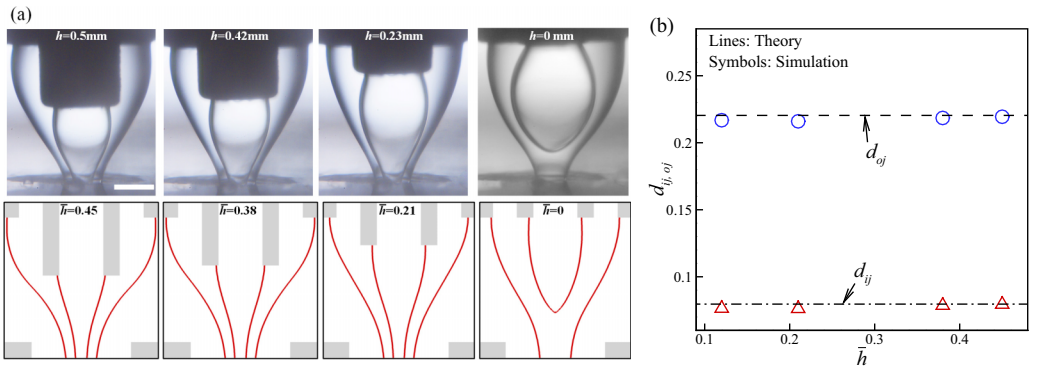

FIG. 8. (a) Coaxial liquid cone profiles as h (nondimensionalized as $\bar{h}$) varies at certain $Q_1 = 15$ ml/h, $Q_2 = 100$ ml/h and $Q_3 = 1400$ ml/h ($q_1 = 0.15$, We $= 0.04$ and $q_2 = 20$). Scale bar: 300 μm. (b) The dimensionless inner and outer jet diameters (d_{ij} and d_{oj}) as $\bar{h}$ varies. The dashed and dash-dotted lines denote the theoretical predictions of Eq. (11), respectively.

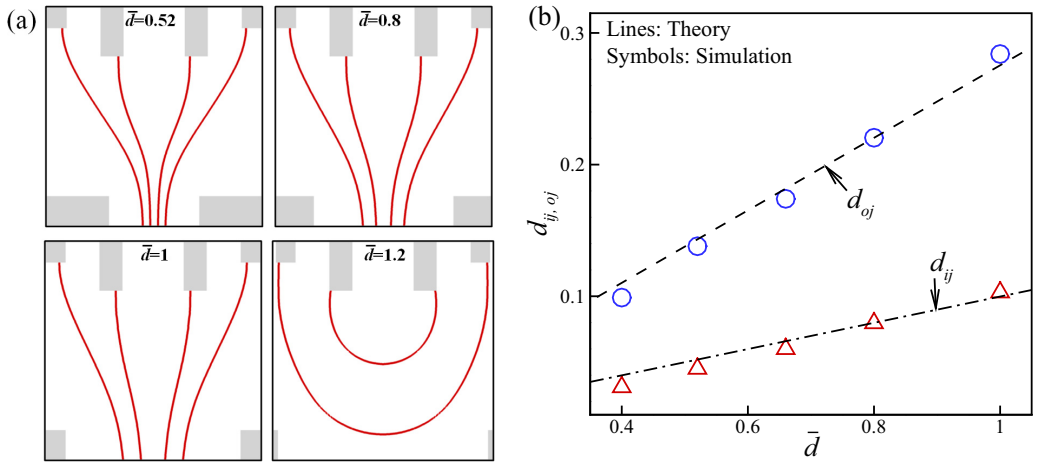

FIG. 9. (a) Numerical coaxial liquid cone profiles as $\bar{d}$ decreases at flow rates $q_1 = 0.15$, We $= 0.04$, and $q_2 = 20$. Scale bar: 300 μm. (b) The dimensionless inner and outer jet diameters (d_{ij} and d_{oj}) as $\bar{d}$ varies. The dashed and dash-dotted lines denote the theoretical predictions of Eq. (11), respectively.

showing that the outer jet diameter increases with We while the inner jet diameter decreases with We. A good agreement can be reached with the theoretical prediction of with Eq. (11). The effect of liquid flow rate Q_3 for the outermost focusing liquid (nondimensionalized as q_2) on the coaxial liquid cone is further studied in Fig. 6(a). Similar to the variation of Q_2, under a small value of Q_3 the coaxial liquid cone is unstable and present a temporally vibrating behavior. As Q_3 increases, a stable

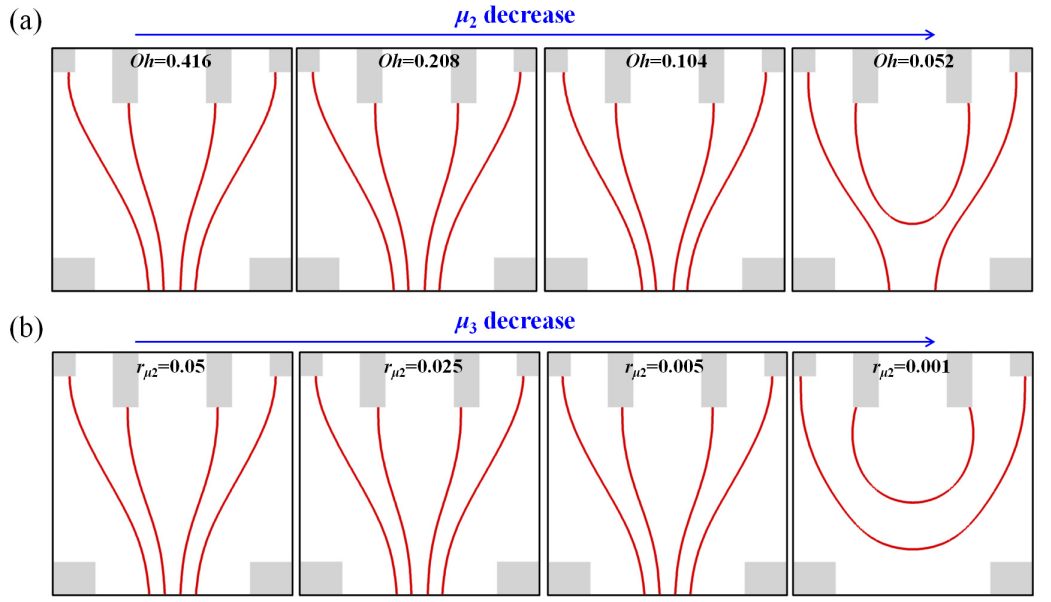

FIG. 10. Numerical coaxial liquid cone profiles as (a) μ_2 varies singly, corresponding to the change of Oh at certain values of Oh$r_{\mu 1}$ = Oh$r_{\mu 2}$ = 0.0052; and (b) μ_2 varies singly, corresponding to the change of $r_{\mu 2}$ at certain Oh = 0.208 and $r_{\mu 1} = 0.025$. The liquid flow rates of triple phases are $q_1 = 0.15$, We $= 0.04$, and $q_2 = 20$.

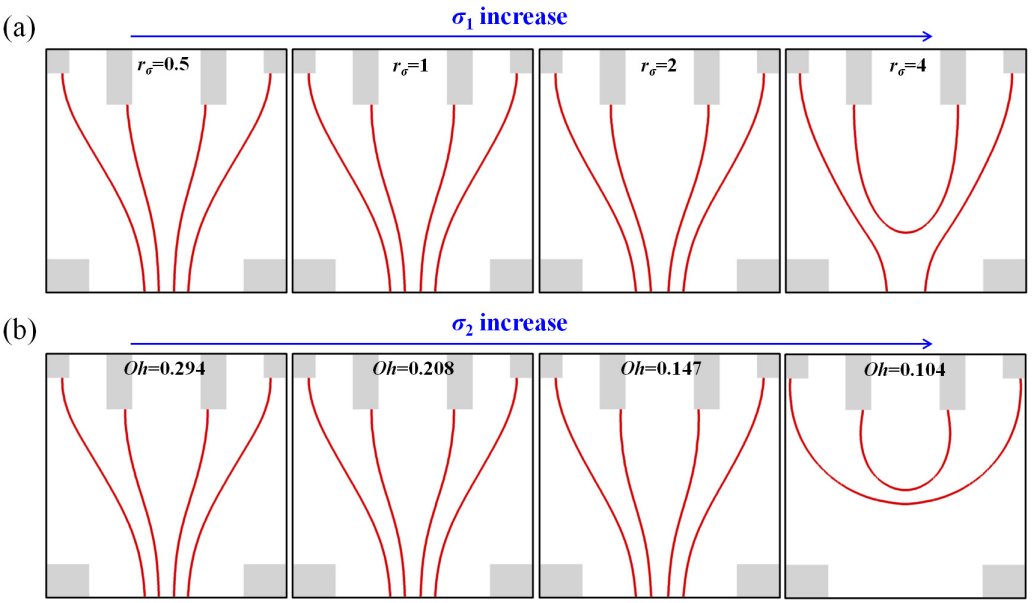

FIG. 11. Numerical coaxial liquid cone profiles as (a) σ_1 varies singly, corresponding to the change of r_σ at Oh $= 0.208$; and (b) σ_2 varies singly, corresponding to the change of Oh at certain values of Oh$/\sqrt{r_\sigma} = 0.208$. The liquid flow rates of triple phases are $q_1 = 0.15$, Re $= 0.957$, and $q_2 = 20$.

coaxial cone-jet configuration can be established, and the diameters of outer and inner jets gradually decrease with Q_3 increasing. The numerical measurements of the dimensionless jet diameters are plotted in Fig. 6(b), which is also consistent with the theoretical results of Eq. (11). The effects of main geometrical parameters of CFF device, including the distance H between the outer capillary tube and the orifice, the inner tube outset h, and the orifice diameter d, on the instability of the coaxial liquid cone are also analyzed. Figure 7(a) reveals that H (nondimensionalized as $\bar{H}$) has a significant influence on the stability and morphology of the coaxial cone. When H is relatively large, the outer and inner liquid cone will both present an unsteady vibrating manner, which is consistent with the theoretical prediction of Eq. (12). As H gradually decreases, the coaxial liquid cone is able to maintain a stable profile. Moreover, it is observed that the liquid cone interfaces will gradually transfer from a convex shape at large values of H to a concave shape at low values of H. The reason lies in that as the flow velocity far from the focusing orifice is relatively low [shown in Fig. 3(a)], the interface would present a droplet-like convex shape due to the dominance of interfacial tension. When H is small, the shear stress close to the orifice will significantly stretch the interface and thus present a concave shape. The diameters of the outer and inner liquid jets measured in numerical simulations under different $\bar{H}$ are shown in Fig. 7(b), suggesting that $\bar{H}$ hardly affects d_{oj} and d_{ij}, and the results are in good agreement with the theoretical predictions. Figure 8(a) further considers the effect of h (nondimensionalized as $\bar{h}$) on the coaxial liquid cone. When h is relatively small, which corresponds to a large distance between the inner tube and the orifice (denoted by $H - h$), the inner cone is unstable and presents a vibrating manner, which is consistent with the theoretical prediction of Eq. (12). The vibration of inner cone terminates the formation of a stable coaxial jet downstream the orifice. As h gradually increases, the distance between the inner tube and the orifice $(H - h)$ decreases and the coaxial liquid cone is able to maintain a stable profile. The jet diameters under different $\bar{h}$ for a stable coaxial cone are shown in Fig. 8(b), suggesting that $\bar{h}$ would not affect the values of d_{oj} and d_{ij}.

Due to the integration of the experimental device, the orifice diameter can not be changed optionally. Therefore, the effect of orifice diameter on the coaxial liquid cone is studied numerically,

as presented in Fig. 9(a). An increase of $\bar{d}$ is able to reduce the driving effect of the focusing liquid on the outer interface by decreasing the difference of their flow velocities, making the cone enlarged, and finally destabilize the cone, which is also well predicted by Eq. (12). Moreover, Fig. 9(b) shows that the diameters of inner and outer liquid jets increase linearly with $\bar{d}$ increasing in the situation of maintaining an always stable cone, and the numerical results agree well with the theoretical predictions of Eq. (11). The effects of liquid physical properties on the cone instability are a little complicated. The numerical results indicate that the liquid viscosities μ_3 and μ_2, and the interfacial tensions σ_2 and σ_1 play a significant role on the instability of coaxial liquid cone. For simplification, the single variation of main physical properties is considered in numerical simulations by keeping the rest parameters constant. According to the definition of dimensionless parameters, the single change of μ_2 corresponds to the variation of Oh at certain values of Oh$r_{\mu 1}$ and Oh$r_{\mu 2}$, and single change of μ_3 corresponds to the variation of $r_{\mu 2}$ at certain values of Oh and $r_{\mu 1}$, respectively. Figure 10(a) considers the effect of μ_2 on the coaxial cone profiles by changing the value of Oh, in which $r_{\mu 1}$ and $r_{\mu 2}$ are also changed by maintaining the values of Oh$r_{\mu 1}$ and Oh$r_{\mu 2}$. It is found that when Oh is small (i.e., Oh $= 0.052$), which corresponds to a low value of μ_2, the inner cone presents an unstable behavior due to the insufficient shear stress provided by the shell liquid. This observation agrees well with the theoretical prediction of Eq. (12). As Oh gradually increases, which corresponds to the increase of μ_2, the shear stress of the shell liquid is able to overcome the interfacial tension and a stable inner cone can be established. The variation of μ_3 (nondimensionalized by $r_{\mu 2}$) is considered in Fig. 10(b). When $r_{\mu 2}$ is small (i.e., $r_{\mu 2} = 0.001$), which corresponds to a low value of μ_3, the coaxial liquid cone presents an unstable behavior as the shear stress of the focusing liquid is relatively low. Actually, the nondimensional analysis has indicated that the decrease of μ_3 will cause the instability of the outer cone, and the vibration of outer interface would certainly lead to the accompanying vibration of the inner cone. As $r_{\mu 2}$ (μ_3) gradually increases, the stable coaxial liquid cone can be maintained. It is clearly seen in Fig. 10 that once the coaxial cone gets stable as μ_2 or μ_3 increases, the profiles of the cone interface only vary slightly with liquid viscosities changing.

Apart from the liquid viscosities, the variation of interfacial tensions are further considered in Fig. 11. It is notable that the single change of inner interfacial tension σ_1 corresponds to the variation of r_σ at certain values of Oh and We, and the single change of outer interfacial tension σ_2 corresponds to the variation of Oh at certain values of Re ($= \sqrt{\text{We}}/\text{Oh}$) and Oh$/\sqrt{r_\sigma}$, respectively. Figure 11(a) shows that the inner liquid cone presents an unstable behavior at relatively high σ_1 (nondimensionlized as r_σ), which is consistent with the theoretical prediction of Eq. (12). As σ_1 decreases, the coaxial liquid cone is able to maintain a stable profile. Once the cone gets stable, it is observed that σ_1 affects the cone profiles slightly. The variation of σ_2 is considered in Fig. 11(b), where a decrease of Oh denotes the increase of σ_2. It is observed that the coaxial cone is unstable and vibrates continuously at relatively high σ_2 due to the domination of interfacial tension. According to the theoretical prediction of Eq. (12), a large σ_2 would cause the instability of outer liquid cone, which would lead to the vibration of inner cone subsequently. The coaxial liquid cone gradually gets stable as σ_2 decreases, and the morphology of the stable cone can hardly be affected by the interfacial tension.

D. Recirculation flow inside the liquid cone

The interfacial instability and morphology of the coaxial liquid cone are directly correlated to the flow fields within the cone. To visualize the flow field characteristics of the cone, the tracing particles (hollow glass beads with average diameter of 20 μm) are added in the inner liquid, and the motion of particles is recorded by the high-speed video camera in experiments. As the average density of the tracing particles ($\approx$1030 kg m^{-3}) is very close to that of the inner liquid, the particles can suspend uniformly with negligible agglomeration and sedimentation, which enables a favorable visualization effect. Numerical results are also utilized for quantitative analysis on the flow fields. Figure 12(a) shows a group of experimental and numerical results (see the upper and

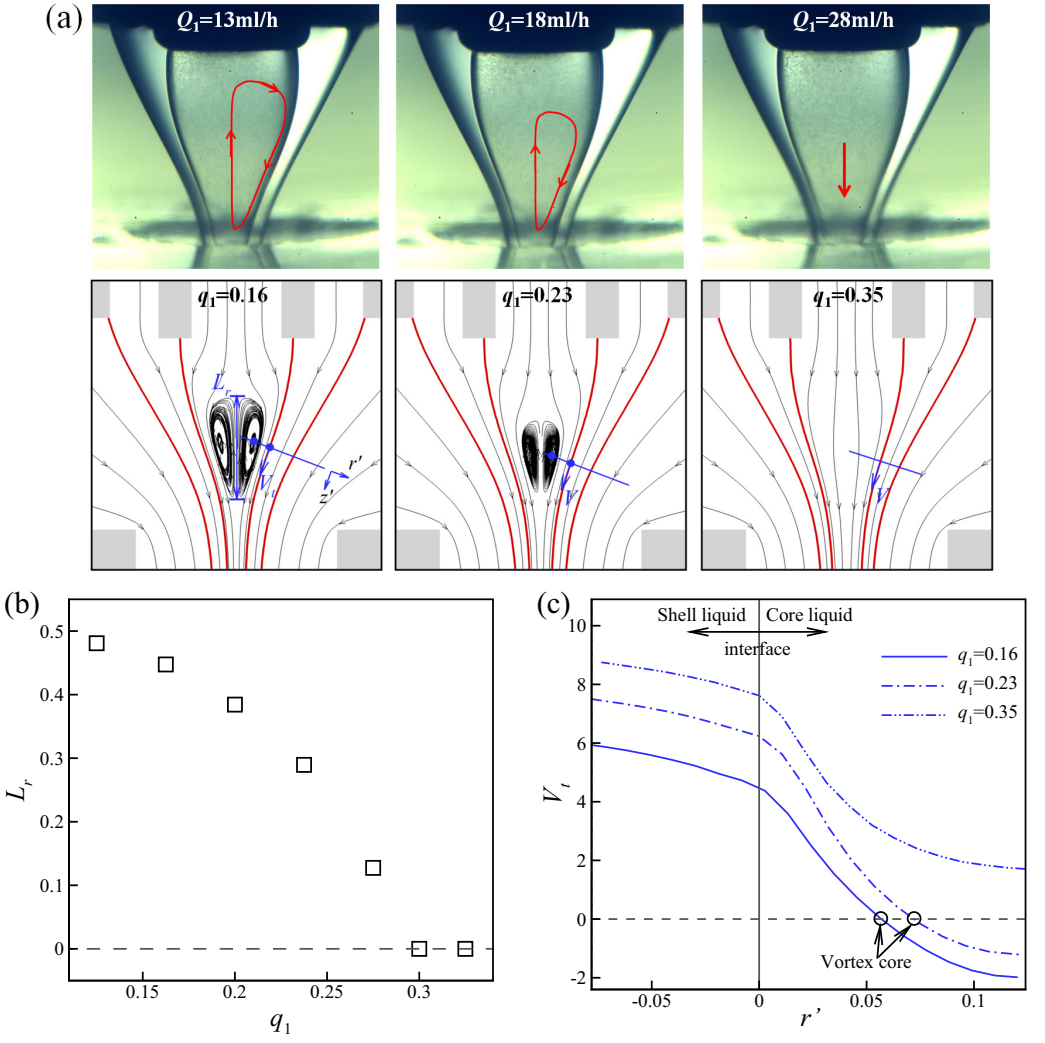

FIG. 12. (a) Experimental visualization of recirculation cell (RC) and the corresponding numerical results as Q_1 (q_1) varies under certain values of $Q_2 = 80$ ml/h and $Q_3 = 1600$ ml/h (We $= 0.025$ and $q_2 = 20$). (b) Measured length of RC at the symmetry axis as q_1 varies. (c) Distributions of tangential velocity along the r' direction at different q_1.

lower parts, respectively), where the flow rates of shell and focusing liquids are $Q_2 = 80$ ml/h and $Q_3 = 1600$ ml/h and the flow rate of core liquid Q_1 varies, i.e., 13 ml/h, 18 ml/h, and 28 ml/h, respectively. The single variation of Q_1 corresponds to the change of q_1 in numerical simulations. It is observed that a recirculation cell (RC) occurs inside the inner cone for relatively low Q_1 (e.g., $Q_1 = 13$ ml/h, corresponding to $q_1 = 0.16$). The RC leads to the backflow of tracing particles where the flow direction at the symmetry axis is opposite to that in the capillary tube. Due to the light refraction on the curved interfaces, the size of RC observed in experiments is obviously larger than that in numerical simulations. As Q_1 increases ($Q_1 = 18$ ml/h, corresponding to $q_1 = 0.23$), the size of RC gradually decreases and finally vanishes at a relatively high value of Q_1 ($Q_1 = 28$ ml/h, corresponding to $q_1 = 0.35$). It should be emphasized that the RC is a temporally steady configuration, and its size hardly changes with time. Previous study carried

out by Gañán-Calvo *et al.* [45] has proved that the characteristic mass diffusion time is much longer than the characteristic time associate to the recirculation flow; therefore, the mass diffusion between RC and the outer environment is very weak. Moreover, the Brownian motion can also be ignored as the size of tracing particle is much larger than the typical length scale for the observation of Brownian motion. The particles trapped inside the RC rotate persistently with very weak substance exchanging with the outer environment. The flow dynamics as Q_1 varies can be seen in Supplemental Videos S1 ~S3 for the flow dynamics at the flow rate $Q_1 = 13$, 18, and 28 ml/h, respectively [46]. In experiments, the backlighting illumination is used, in which the depth of focus brings integration effect on the observation of particle movement. To minimize the depth of focus, the microscope (Leica Z16 APO, Germany) is adjusted to the largest magnification and fully opening the diaphragm during experimental observation. In this condition, an approximate value of depth of focus $\Delta L \approx 40$ μm can be obtained. As ΔL is obviously smaller than the transverse width w of the RC [e.g., the transverse width of RC for the case $q_1 = 0.16$ and 0.23 in Fig. 12(a) is 238 μm and 170 μm, respectively], the particle movement within the coaxial liquid cone can be clearly observed, efficiently avoiding the three-dimensional integration effect along the light illumination path.

The length L_r of RC measured along the symmetry axis [see the definition in the lower subgraph in Fig. 12(a)] as Q_1 gradually changes is shown in Fig. 12(b), which suggests that L_r will decrease gradually with Q_1 increasing and therefore a larger RC occurs inside the cone. At the vortex core of the RC, the local flow velocity corresponds to zero. Then the tangential velocity V_t both inside and outside the interface perpendicular to the interface of inner cone is sketched in Fig. 12(a) for the case $q_1 = 0.16$ and 0.23. For comparison, we also extract the tangential velocity for the case $q_1 = 0.35$ at the same z position with the case $q_1 = 0.23$. The distributions of tangential velocity for three cases are shown in Fig. 12(c). As the viscosity of the core liquid (distilled water with viscosity of 0.001 Pa s) is much lower than that of the shell liquid (silicone oil with viscosity of 0.04 Pa s), the velocity gradient inside the inner liquid cone would be much higher than that outside the cone to ensure the balance of shear stress on both sides of the interface. For the case $q_1 = 0.16$, as the flow velocity is relatively low, the tangential velocity inside the cone drops quickly and becomes opposite some distance away from the interface, causing the appearance of backfow inside the cone. As q_1 increases to 0.23, the velocity for both the core and shell liquids increases, and the distance between the vortex core and the interface increases significantly, thus decreasing the size of RC. When q_1 increases to 0.35, the velocity both inside and outside the interface increases simultaneously and maintains positive invariably, making the backflow disappear inside the cone.

The effects of shell and focusing liquid flow rates (Q_2 and Q_3, nondimensionalized as We and q_2) on the RC formation are studied in Figs. 13(a) and 13(b), respectively. Figure 13(a) shows that an increase of We under certain $\mathrm{We}q_1^2$ and $\mathrm{We}q_2^2$ (corresponding to the single increase of Q_2 under certain Q_1 and Q_3) changes the length of RC insignificantly. Moreover, an increase of shell liquid flow rate can squeeze the inner cone to a narrower size, which causes the position of RC shifting upstream. Similar to Fig. 12, we analyze the tangential velocity V_t on both sides of the interface, as shown in Fig. 13(c). It is observed that the velocity distributions almost coincide under different We, suggesting a self-similar characteristic of the flow around the RC. Therefore, the size of RC barely varies with We. Likewise for the situations as q_2 decreases under certain We and q_1 (corresponding to the decrease of Q_3 under certain Q_1 and Q_2), the length L_r maintains almost unchanged, as shown in Fig. 13(b). The position of RC would also shift upstream slightly as q_2 increases. Considering the tangential velocity V_t on both sides of the interface, as shown in Fig. 13(d), it is found that the velocity distribution almost coincides under different q_2 and a self-similar characteristic can be reached. It is notable that the effect of liquid flow rates on the size of RC in CFF is obviously different from that in SFF [29]. For the single liquid cone in SFF, an increase on the flow rate of focusing liquid can enlarge the size of RC significantly; while for the coaxial cone in CFF, the increase on the flow rates of either shell or focusing liquid hardly affect the size of RC within the inner liquid cone.

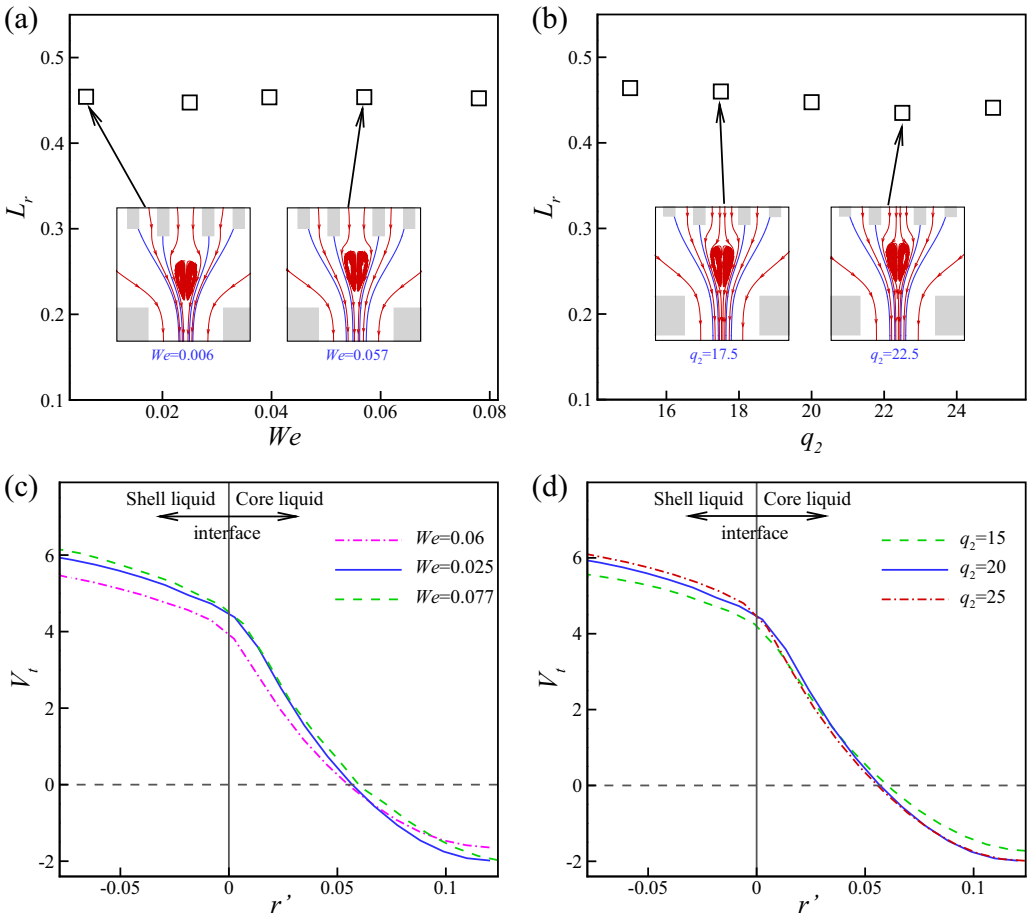

FIG. 13. Length of RC as (a) We varies at certain We$q_1 = 0.001$ and We$q_2 = 7.76$ and (b) q_2 varies at certain We $= 0.025$ and $q_1 = 0.163$. Distributions of tangential velocity along the r' direction at different (c) We and (d) q_2.

IV. CONCLUSION

The direct numerical simulations are combined with experimental measurements to study the effects of various process parameters on the coaxial liquid cone in an axisymmetric liquid-driven coflow focusing process. The startup process of the outer and inner cone interfaces within a stable focusing stream is analyzed. Nondimensional analysis that considers the balance between the viscous shear stress and the interfacial tension at local inner and outer cones is used to consider the coaxial cone instability affected by various parameters jointly. For example, the increase of the triple liquids flow rates, and the increase of liquid viscosities can lead to a more stable coaxial liquid cone; while the increase of the distance between the capillary tube and the orifice, and the increase of the orifice diameter and the increase of interfacial tensions can promote the instability of the coaxial cone. The experimental and numerical results validate the effect of parameters shown by the nondimensional analysis, and further illustrate the variations of cone morphology and jet diameter as the control parameters change. It is found that a recirculation cell would occur inside the liquid cone, which is closely related to the the balance of local shear stress on the cone interface. The increase of core liquid flow rate can decrease the size of recirculation cell, while the variation of shell and focusing liquid flow rates only affects the size of recirculation cell slightly. This study provides a

valuable qualitative understanding of the role of all parameters involved in the coaxial liquid cone in CFF process, contributes to the process optimization on the formation of stable coaxial cone-jet configuration and facilitates the applications of coflow focusing in producting microcapsules.

ACKNOWLEDGMENTS

This work was supported by the National Natural Science Foundation of China (Grants No. 11902318, No. 12027801, and No. 11621202), the Youth Innovation Promotion Association CAS (Grant No. 2018491), the Strategic Priority Research Program of the Chinese Academy of Sciences (Grant No. XDB22040103), the open fund of the Key Laboratory of Aero Engine Extreme Manufacturing Technology of Zhejiang Province, and the Fundamental Research Funds for the Central Universities. The authors thank Mr. R. Qiao, J. Guo, X. Xu, and Ms. C. Li for their help in the experiments.

[1] A. M. Gañán-Calvo, J. M. Montanero, L. Martin-Banderas, and M. Flores-Mosquera, Building functional materials for health care and pharmacy from microfluidic principles and flow focusing, Adv. Drug Deliv. Rev. **65**, 1447 (2013).

[2] P. A. Zhu and L. Q. Wang, Passive and active droplet generation with microfluidics: A review, Lab Chip **17**, 34 (2017).

[3] J. Guerrero, Y. W. Chang, A. A. Fragkopoulos, and A. Fernandez-Nieves, Capillary-based microfluidics-coflow, flow-focusing, electro-coflow, drops, jets, and instabilities, Small **16**, 1904344 (2020).

[4] A. Barrero and I. G. Loscertales, Micro- and nanoparticles via capillary flows, Annu. Rev. Fluid Mech. **39**, 89 (2007).

[5] M. A. Herrada, J. M. Montanero, C. Ferrera, and A. M. Gañán-Calvo, Analysis of the dripping-jetting transition in compound capillary jets, J. Fluid Mech. **649**, 523 (2010).

[6] Z. Q. Zhu, T. Si, and R. X. Xu, Microencapsulation of indocyanine green for potential applications in image-guided drug delivery, Lab Chip **15**, 646 (2015).

[7] K. Mu, R. Qiao, T. Si, X. Q. Chen, and H. Ding, Interfacial instability and transition of jetting and dripping modes in a coflow focusing process, Phys. Fluids **33**, 052118 (2021).

[8] A. S. Utada, E. Lorenceau, D. R. Link, P. D. Kaplan, H. A. Stone, and D. A. Weitz, Monodisperse double emulsions generated from a microcapillary device, Science **308**, 537 (2005).

[9] M. Robert de Saint Vincent and J.-P. Delville, Fragmentation mechanisms of confined coflowing capillary threads revealed by active flow focusing, Phys. Rev. Fluids **1**, 043901 (2016).

[10] S. L. Anna, Droplets and bubbles in microfluidic devices, Annu. Rev. Fluid Mech. **48**, 285 (2016).

[11] K. Y. He, F. Campo-Cortés, M. Goral, T. López-León, and J. M. Gordillo, Micron-sized double emulsions and nematic shells generated via tip streaming, Phys. Rev. Fluids **4**, 124201 (2019).

[12] V. G. Agarwal, R. Singh, S. S. Bahga, and A. Gupta, Dynamics of droplet formation and flow regime transition in a t-shaped microfluidic device with a shear-thinning continuous phase, Phys. Rev. Fluids **5**, 044203 (2020).

[13] T. Cubaud, B. Conry, X. Y. Hu, and T. Dinh, Diffusive and capillary instabilities of viscous fluid threads in microchannels, Phys. Rev. Fluids **6**, 094202 (2021).

[14] J. Montanero and A. M. Gañán-Calvo, Dripping, jetting and tip streaming, Rep. Prog. Phys. **83**, 097001 (2020).

[15] Q. Wu, C. Y. Yang, G. L. Liu, W. H. Xu, Z. Q. Zhu, T. Si, and R. X. Xu, Multiplex coaxial flow focusing for producing multicompartment janus microcapsules with tunable material compositions and structural characteristics, Lab Chip **17**, 3168 (2017).

[16] J. Y. Liu, Y. Zhong, K. Mu, T. L. Han, H. G. Zhang, and T. Si, A self-healing lithium–sulfur battery using gel-infilled microcapsules, Appl. Energ. Mater. **4**, 6749 (2021).

[17] A. M. Gañán-Calvo, Generation of Steady Liquid Microthreads and Micron-Sized Monodisperse Sprays in Gas Streams, Phys. Rev. Lett. **80**, 285 (1998).

[18] A. Chauhan, C. Maldarelli, D. T. Papageorgiou, and D. S. Rumschitzki, The absolute instability of an inviscid compound jet, J. Fluid Mech. **549**, 81 (2006).
[19] K. Mu, T. Si, E. Q. Li, R. X. Xu, and H. Ding, Numerical study on droplet generation in axisymmetric flow focusing upon actuation, Phys. Fluids **30**, 012111 (2018).
[20] C. Y. Yang, R. Qiao, K. Mu, Z. Q. Zhu, R. X. Xu, and T. Si, Manipulation of jet breakup length and droplet size in axisymmetric flow focusing upon actuation, Phys. Fluids **31**, 091702 (2019).
[21] R. Bocanegra, J. L. Sampedro, A. M. Gañán-Calvo, and M. Marquez, Monodisperse structured multi-vesicle microencapsulation using flow-focusing and controlled disturbance, J. Microencapsul. **22**, 745 (2005).
[22] N. N. Wang, C. Semprebon, H. H. Liu, C. H. Zhang, and H. Kusumaatmaja, Modelling double emulsion formation in planar flow-focusing microchannels, J. Fluid Mech. **895**, A22 (2020).
[23] K. Mu, H. Ding, and T. Si, Experimental and numerical investigations on interface coupling of coaxial liquid jets in coflow focusing, Phys. Fluids **32**, 042103 (2020).
[24] T. X. Zhang, X. Zou, L. Xu, D. W. Pan, and W. X. Huang, Numerical investigation of fluid property effects on formation dynamics of millimeter-scale compound droplets in a coflowing device, Chem. Eng. Sci. **229**, 116156 (2021).
[25] A. M. Gañán-Calvo, R. Gonzalez-Prieto, P. Riesco-Chueca, M. A. Herrada, and M. Flores-Mosquera, Focusing capillary jets close to the continuum limit, Nat. Phys. **3**, 737 (2007).
[26] A. Evangelio, F. Campo-Cortes, and J. M. Gordillo, Simple and double microemulsions via the capillary breakup of highly stretched liquid jets, J. Fluid Mech. **804**, 550 (2016).
[27] M. A. Herrada, A. M. Gañán-Calvo, A. Ojeda-Monge, B. Bluth, and P. Riesco-Chueca, Liquid flow focused by a gas: Jetting, dripping, and recirculation, Phys. Rev. E **78**, 036323 (2008).
[28] J. M. Montanero, N. Rebollo-Munoz, M. A. Herrada, and A. M. Gañán-Calvo, Global stability of the focusing effect of fluid jet flows, Phys. Rev. E **83**, 036309 (2011).
[29] K. Mu, R. Qiao, J. F. Guo, C. Y. Yang, Y. F. Wu, and T. Si, Parametric study on stability and morphology of liquid cone in flow focusing, Int. J. Multiphas. Flow **135**, 103507 (2021).
[30] C. Y. Zhang, H. Ding, P. Gao, and Y. L. Wu, Diffuse interface simulation of ternary fluids in contact with solid, J. Comput. Phys. **309**, 37 (2016).
[31] D. Jacqmin, Calculation of two-phase Navier–Stokes flows using phase-field modeling, J. Comput. Phys. **155**, 96 (1999).
[32] P. Zuo and Y. P. Zhao, A phase field model coupling lithium diffusion and stress evolution with crack propagation and application in lithium ion batteries, Phys. Chem. Chem. Phys. **17**, 287 (2015).
[33] H. Ding, P. D. M. Spelt, and C. Shu, Diffuse interface model for incompressible two-phase flows with large density ratios, J.Comput. Phys. **226**, 2078 (2007).
[34] A. J. Acero, C. Ferrera, J. M. Montanero, and A. M. Gañán-Calvo-Calvo, Focusing liquid microjets with nozzles, J. Micromech. Microeng. **22**, 065011 (2012).
[35] Z. B. Wang, T. Q. Zhai, H. Y. Liu, Y. A. Huang, and W. W. Deng, Two dimensional liquid flow focusing, Phys. Fluids **32**, 042104 (2020).
[36] A. M. Gañán-Calvo and J. M. Montanero, Revision of capillary cone-jet physics: Electrospray and flow focusing, Phys. Rev. E **79**, 066305 (2009).
[37] E. J. Vega, J. M. Montanero, and M. A. Herrada, Global and local instability of flow focusing: The influence of the geometry, Phys. Fluids **22**, 064105 (2010).
[38] J. M. Gordillo, A. Sevilla, and F. Campo-Cortés, Global stability of stretched jets: Conditions for the generation of monodisperse micro-emulsions using coflows, J. Fluid Mech. **738**, 335 (2014).
[39] F. Cruz-Mazo, M. A. Herrada, A. M. Gañán-Calvo, and J. M. Montanero, Global stability of axisymmetric flow focusing, J. Fluid Mech. **832**, 329 (2017).
[40] M. G. Cabezas, N. Rebollo-Muñoz, M. Rubio, M. A. Herrada, and J. M. Montanero, Global stability analysis of axisymmetric liquid-liquid flow focusing, J. Fluid Mech. **909**, A10 (2021).
[41] S. L. Anna and H. C. Mayer, Microscale tipstreaming in a microfluidic flow focusing device, Phys. Fluids **18**, 121512 (2006).
[42] W. Lee, L. M. Walker, and S. L. Anna, Role of geometry and fluid properties in droplet and thread formation processes in planar flow focusing, Phys. Fluids **21**, 032103 (2009).

[43] E. Castro-Hernandez, V. Gundabala, A. Fernandez-Nieves, and J. M. Gordillo, Scaling the drop size in coflow experiments, New J. Phys. **11**, 075021 (2009).

[44] A. M. Gañán-Calvo and P. Riesco-Chueca, Jetting-dripping transition of a liquid jet in a lower viscosity coflowing immiscible liquid: The minimum flow rate in flow focusing, J. Fluid Mech. **553**, 75 (2006).

[45] A. M. Gañán-Calvo, C. Ferrera, M. Torregrosa, M. A. Herrada, and M. Marchand, Experimental and numerical study of the recirculation flow inside a liquid meniscus focused by air, Microfluid Nanofluid **11**, 65 (2011).

[46] See Supplemental Material at http://link.aps.org/supplemental/10.1103/PhysRevFluids.7.024001 for the videos showing the flow dynamics at the flow rate $q_1 = 13$, 18, and 28 ml/h, respectively.